Journal of Marine Science and Technology

Volume 26 | Issue 3 Article 2

THE THREE-DIMENSIONAL FLOW SIMULATION OF A FLAPPING WING

Lung-Jieh Yang
Mechanical and Electro-Mechanical Engineering, Tamkang University, Taiwan, R.O.C, ljyang@mail.tku.edu.tw

Ai-Lien Feng
Mechanical and Electro-Mechanical Engineering, Tamkang University, Taiwan, R.O.C.

Hsi-Chun Lee
Mechanical and Electro-Mechanical Engineering, Tamkang University, Taiwan, R.O.C

Balasubramanian Esakki
Mechanical Engineering, Veltech Dr. RR & Dr. SR University, Chennai, India

Wei He
School of Automation and Electrical Engineering, University of Science and Technology Beijing (USTB), Beijing, China

Follow this and additional works at: https://jmstt.ntou.edu.tw/journal

 Part of the Engineering Commons

Recommended Citation

Yang, Lung-Jieh; Feng, Ai-Lien; Lee, Hsi-Chun; Esakki, Balasubramanian; and He, Wei (2018) "THE THREE-DIMENSIONAL FLOW SIMULATION OF A FLAPPING WING," *Journal of Marine Science and Technology*: Vol. 26: Iss. 3, Article 2.
DOI: DOI: 10.6119/JMST.201806_26(3).0002
Available at: https://jmstt.ntou.edu.tw/journal/vol26/iss3/2

This Research Article is brought to you for free and open access by Journal of Marine Science and Technology. It has been accepted for inclusion in Journal of Marine Science and Technology by an authorized editor of Journal of Marine Science and Technology.

THE THREE-DIMENSIONAL FLOW SIMULATION OF A FLAPPING WING

Acknowledgements

The authors sincerely thank the financial support from Ministry of Science and Technology (MOST-106-2221- E-032-040) Taiwan and the help from Mr. Ting-Hsiung Huang.

This research article is available in Journal of Marine Science and Technology: https://jmstt.ntou.edu.tw/journal/vol26/iss3/2

Journal of Marine Science and Technology, Vol. 26, No. 3, pp. 297-308 (2018)
DOI: 10.6119/JMST.2018.06_(3).0002

THE THREE-DIMENSIONAL FLOW SIMULATION OF A FLAPPING WING

Lung-Jieh Yang[1], Ai-Lien Feng[1], Hsi-Chun Lee[1], Balasubramanian Esakki[2], and Wei He[3]

Key words: flapping wing micro-air-vehicle (FWMAV), fluid-structure interaction (FSI), computational fluid dynamics (CFD), COMSOL Multiphysics.

ABSTRACT

This study investigates three-dimensional (3D) flow fields around a flapping wing with a span of 20 cm. Numerical simulations are performed by varying the simulation mesh density for a half-flapping-wing profile with wind tunnel domain for flapping stroke angles of 53° and 90°. Wind velocities ranging from 1 to 3 m/s, variation in flapping frequency of 14-15 Hz, and corresponding lift characteristics are obtained. Comparative evaluation of numerical and experimental lift force data reveals the translational and rotational lift phenomena of Dickinson's mechanisms. The stream line that flows over the 3D wing profile is found to be in good agreement with the existing smoke trace experimental data. The motions of a flapping wing obtained through 3D stereo photography and COMSOL Multiphysics simulation are compared and the aerodynamic characteristics are exploited. The streamwise and spanwise 3D velocity fields with intercepting planes at three chord sections are explored, and the reverse Kármán vortex sheet is observed. The comparison of the simulation and experimental results for a 3D flapping wing provides insight into the motion characteristics of a flapping wing and flapping wing aerodynamic analysis of micro air vehicles.

I. INTRODUCTION

Flapping wing micro air vehicles (FWMAVs), or ornithopters, have several advantages compared with vehicles with rotary and fixed wings because of their maneuverability, high power efficiency at low flight speeds, and durability. Flapping wing vehicles have attracted research attention because of the behavior they can exhibit, such as hovering, low-speed flight, navigating in tight environments, short takeoffs and landings, perching, and efficient gliding. FWMAVs are capable of adapting to changing aerodynamic situations through their flight characteristics. They can vary their angle of attack (AOA), wingtip trace pattern, wing area, and flapping frequency, and their feather orientation can be adjusted to achieve cruising and forward flight. They are also capable of accomplishing several missions in indoor as well as outdoor locations and exhibit exceptional abilities in maneuvering, avoiding obstacles, navigating at low speeds, and switching quickly between forward and hovering flight.

In 2011, AeroVironment Inc. and the US Defense Advanced Research Projects Agency announced a 6-year project, named the hummingbird hovering flapping machine ("Nano Hummingbird" MAV), which has a 16.5-cm wingspan and wing stroke angle of 210° with a 30-Hz flapping frequency. The machine can hover for up to 660 s and has a maximum flight speed of 24 km/h (Keennon et al., 2012). It was also demonstrated to have semiautonomous control and enable real-time transmission of video signals through an on-board micro camera. On the basis of that research, several researchers began developing microelectromechanical system sensors and actuators for FWMAVs (de Croon et al., 2014; Phan and Park, 2015; Yang et al., 2015), which will play an important role in the near future. Compared with that of quadrotors (Mellinger et al., 2010), the design of FWMAVs is considered challenging because of the miniature size and shape of these vehicles, which have a crucial effect on their aerodynamic performance.

Numerous studies have used computational fluid dynamics (CFD) analysis to investigate flapping in flow with low Reynolds number with reference to two-dimensional (2D) airfoils (Wang, 2000; Wan and Huang, 2008; Chuang et al., 2012). However, the three-dimensional (3D) wing feature of FWMAVs has been rarely evaluated using CFD analysis. A 3D time-varying, flapping wing profile and the inherent fluid-structure interaction (FSI) (Yang, 2012) appears to be beyond the simulation capability of the conventional finite element method (FEM) software such as Fluent, CFDRC, CFX, and StarCD. The flapping wing flow field (Wan and Huang, 2008; Chuang et al., 2012; Niu et al., 2012) has been analyzed by using Fluent and the user-defined function (UDF) to describe the moving boundary of the flapping wing in terms of precisely given functions with respect to time. CFD analysis of a flapping wing through the UDF at

Paper submitted 03/06/17; revised 10/16/17; accepted 03/01/18. Author for correspondence: Lung-Jieh Yang (e-mail: LJYANG@mail.tku.edu.tw).
[1] Mechanical and Electro-Mechanical Engineering, Tamkang University, Taiwan, R.O.C.
[2] Mechanical Engineering, Veltech Dr. RR & Dr. SR University, Chennai, India.
[3] School of Automation and Electrical Engineering, University of Science and Technology Beijing (USTB), Beijing, China.

time t and $(t + \Delta t)$ for solving the Navier-Stokes equations toward convergence for varied flapping strokes is difficult and ineffective because it involves a preprogrammed UDF that is invariant during the whole CFD computation. Moreover, this analysis can be used only for rigid or prescribed wing shapes, and the wings' FSI from past iterations cannot influence future iterations, which is not the case with the real-time scenario of flapping wing motion.

Several CFD computations have been performed to investigate the effect on FSI of 2D flapping wings through experiments such as wind tunnel tests measuring the lift and thrust of flexible flapping wings (Pornsinsirirak et al., 2001; Yang et al., 2012). 3D stereophotographic analysis of the instantaneous profiles of flexible wings (Yang et al., 2013, 2014) and the flow visualization involving smoke track experiments and particle image velocimetry (Dickinson et al., 1999; Hubel and Tropea, 2010) were investigated. The experimental data obtained in these studies not only justified why the corresponding MAVs work successfully (Yang et al., 2009; de Croon et al., 2014; Phan and Park, 2015) but will also enable comparison with newly obtained CFD results for 3D flapping wings.

The 3D, time-varying, and flexible nature of the flapping wing obviously cannot be simply represented by a 2D flow simulation using a UDF. Therefore, 3D flow simulation of the flexible flapping wing is inevitable. COMSOL Multiphysics with FSI capability is computationally powerful, and studies on 2D flapping flows have proved the usefulness of this software (Bucur et al., 2016; Kumar et al., 2016; Nokia Bell Labs Team, 2017). Numerically simulation of the 3D flapping flow has been performed using COMSOL Multiphysics to approximate the actual flapping situation. This 3D simulation of unsteady motion uses the mesh or grid number test for checking the data convergence. The so-called convergence can be determined by observing the periodic behavior of the numerical result of velocity or pressure field after several flapping cycles. The convergence is also confirmed by checking the cycle-averaged lift values. If the numerical results of 3D flapping are converged, they are compared with other experimental data. Comparisons have been made for a 20-cm-span FWMAV named "Golden Snitch" (Shu, 2008; Yang et al., 2009, 2012, 2013, 2014; Chen, 2010) and include the following three parts:

(1) Comparison of the flow patterns, especially the existence of a reverse Kármán vortex in the flow field around a flapping wing, using the results of COMSOL Multiphysics and earlier wind tunnel data (Shu, 2008; Chen, 2010).
(2) Comparison of the time history or waveforms of lift force obtained in CFD analysis and experimental results (Shu, 2008; Chen, 2010).
(3) Comparison of the influence of FSI on the 3D surface profile of the flexible wings over a full flapping cycle due to its aeroelasticity using the results of COMSOL Multiphysics and earlier high-speed stereo photography (Yang et al., 2013, 2014).

This paper obtains the 3D flapping motion flow fields and aerodynamic characteristics of a flapping wing by using the COMSOL Multiphysics platform.

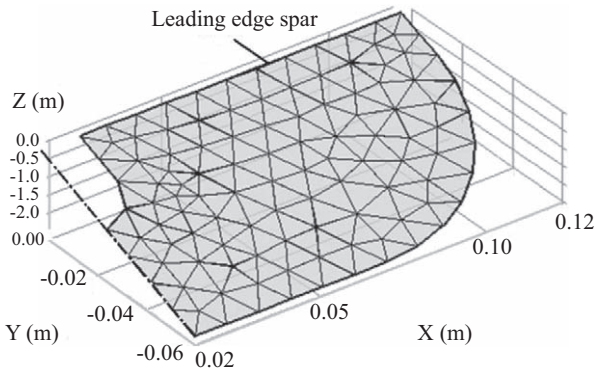

Fig. 1. Right-side half domain of a half flapping wing with its preliminary mesh.

II. NUMERICAL SIMULATION

The simulated subject in the 3D flow field used in this study was the aforementioned 20cm-span FWMAV "Golden Snitch" (Shu, 2008; Yang et al., 2009, 2012, 2013, 2014; Chen, 2010; Yang, 2012), whose wing membrane thickness measured 24 μm and was made of polyethylene terephthalate (PET) (the half wing is shown in Fig. 1). Assuming that the flapping wing was bilaterally symmetrical, only half of the 20-cm span (i.e., 10 cm for the right half wing) was simulated. The FSI governing equations and numerical scheme in COMSOL Multiphysics are outlined as follows:

Fluid Part

Mass conservation:

$$\frac{\partial \rho}{\partial t} + \nabla \cdot (\rho \vec{U}_{fluid}) = 0 \tag{1}$$

Momentum conservation:

$$\rho \frac{\partial \vec{U}_{fluid}}{\partial t} + \rho(\vec{U}_{fluid} \cdot \nabla)\vec{U}_{fluid} =$$
$$\nabla \cdot \left[-P\overline{\overline{I}} + \mu(\nabla \vec{U}_{fluid} + (\nabla \vec{U}_{fluid})^T) - \frac{2}{3}\mu\left(\nabla \cdot \vec{U}_{fluid}\right)\overline{\overline{I}} \right] + \vec{F} \tag{2}$$

Solid Part

Eulerian equation of motion:

$$\rho \frac{\partial^2 \vec{U}_{solid}}{\partial t^2} - \nabla \cdot \overline{\overline{\sigma}} = \vec{F} \tag{3}$$

where $\vec{U}_{fluid}$ denotes the velocity vector of the fluid; $\vec{U}_{solid}$

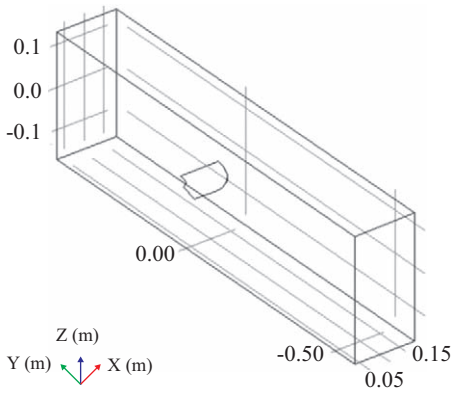

(a) Modelling

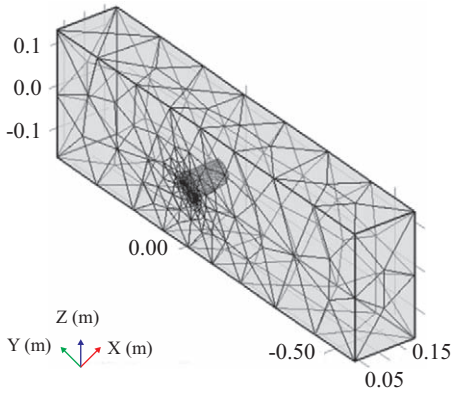

(b) Normal mesh

Fig. 2. Right-side half domain of a single flapping wing with wind tunnel.

denotes the deformation vector of the solid in the problem; P denotes the hydrostatic pressure; $\overline{\overline{\sigma}}$ denotes the stress tensor; $\overline{\overline{I}}$ denoes the identity tensor; and $\vec{F}$ denotes the external force vector. ρ and μ are the fluid density and viscosity, respectively. The upstream velocity regimes are considered to have a speed of 0-3 m/s, and the corresponding Reynolds number is approximately 0-13,380 at a temperatu re of 300 K.

Using COMSOL Multiphysics software to conduct a flow simulation of the flapping wing, the wing membrane coordinates data were first imported, followed by the establishment of a rectangular wind tunnel that served as a surrounding boundary. The wind tunnel was 1 m long, 0.3 m wide, and 0.3 m tall, and was identical to the tunnel used in the previous FWMAV wind tunnel test, depicted in Fig. 2(a) (Yang et al., 2009, 2012, 2013, 2014; Yang, 2012.) To reduce the computation time, the flapping wing was bisected together with the wind tunnel (0.15 m wide), whereby the incision site was configured as a symmetrical plane. Thus, the simulation results could be viewed as a flapping wing flow field simulation of a flapping wing within a wind tunnel, both of which were in complete symmetry. The preliminary mesh of a single flapping wing with wind tunnel are illustrated in Fig. 2(b).

Triangular elements were first set up on the surface of the flapping wing, followed by a scan and conversion of the entire wing surface to establish the mesh configuration of the flapping wing surface (Fig. 1). Subsequently, tetrahedral elements were created according to the wind tunnel space, thereby completing the mesh configuration outlined in Fig. 2(b). After selecting the different mesh sizes in COMSOL and using the corresponding three sets of mesh number distributions, the meshes were divided into Normal (Fig. 2(b)), Fine (Fig. 3(a)), and Extra Fine (Fig. 3(b)) configurations. The number of elements for each set is listed in Table 1, and the complete procedure of CFD analysis in the COMSOL Multiphysics environment is detailed in Table 2.

Simulations are performed for the case of flapping frequency = 14 Hz and upstream wind velocity = 0 m/s with an inclined an-

Table 1. Number of elements in the various mesh configurations.

Mesh Location and Shape	Normal mesh	Fine mesh	Extra Fine mesh
Tetrahedral elements	5,498	6,835	57,341
Triangular elements	850	3,730	9,568
Boundary elements	121	203	397
Endpoint elements	22	22	22
Total elements	6,491	10,790	67,328

Table 2. COMSOL Multiphysics simulation configuration process.

Step	Task Description
1	Input wing membrane coordinates data
2	Rotate the wing (20°) along its wingspan axis into an inclined angle
3	Construct the wind tunnel
4	Form the right-side half domain of the flapping wing and wind tunnel
5	Select the materials for the wind tunnel and flapping wing
6	Set air as the space material for the wind tunnel
7	Input the flapping wing material parameters
8	Set the flapping wing as a linear elastic material
9	Configure the wind tunnel entrance and wind velocity
10	Configure the wind tunnel exit
11	Configure the fixed constraint for the leading edge (L.E.) of the flapping wing
12	Configure the symmetrical plane of the flow field
13	Configure the predetermined time-varying displacement function for the leading edge of the flapping wing
14	Initiate mesh configuration
15	Construct the triangular meshes of the flapping wing
16	Scan the entire flapping wing
17	Initiate conversion
18	Construct the tetrahedral meshes
19	Configure the fineness of the mesh size
20	Complete configuration and initiate FEM calculation

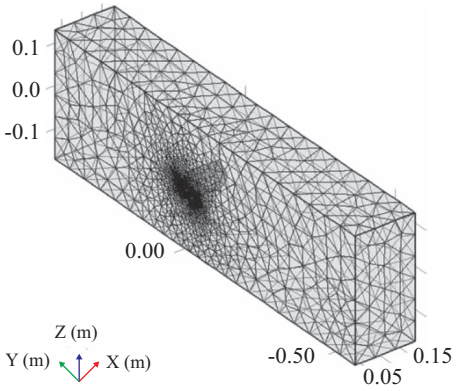

(a) Fine mesh configuration

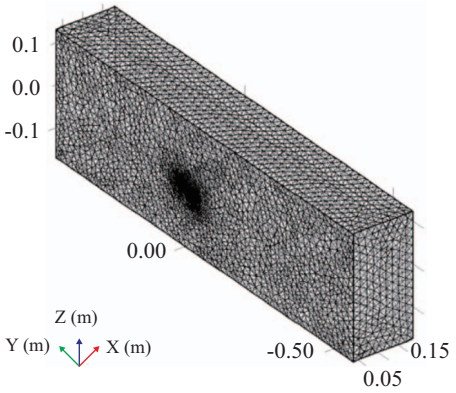

(b) Extra Fine mesh configuration

Fig. 3. Right-side half domain of a single flapping wing with wind tunnel.

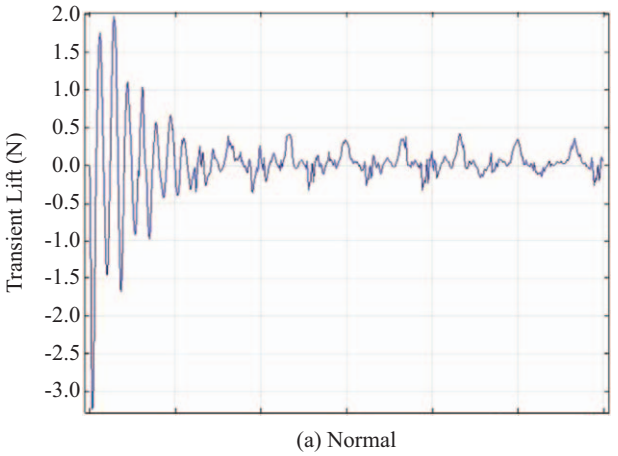

(a) Normal

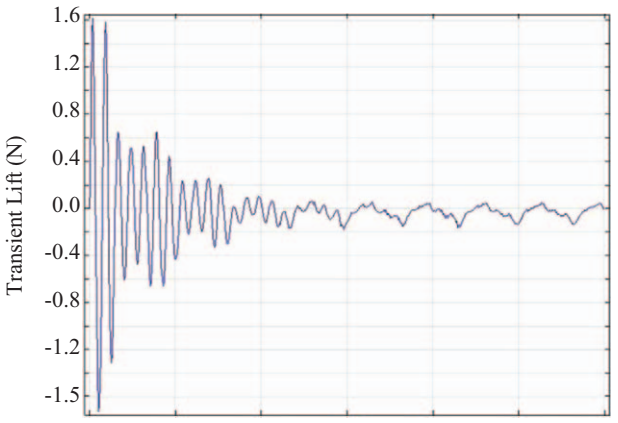

(b) Fine

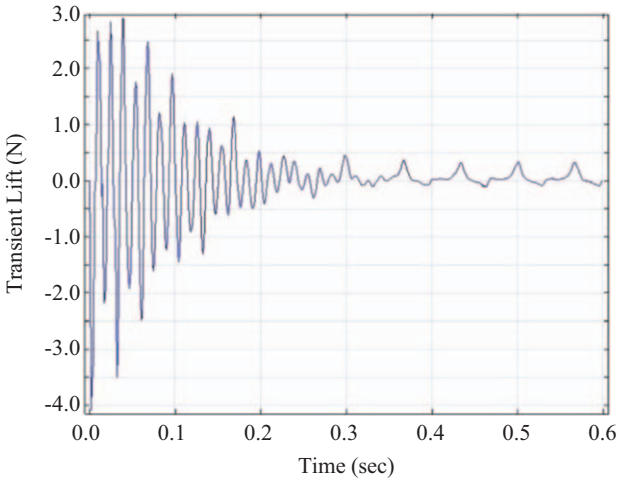

(c) Extra fine

Fig. 4. Lift force diagram different meshes.

gle of 20°. The generated lift force for the three types of mesh is shown in Fig. 4; an increase in the number of elements enhances the lift force, which indicates the obtainment of more favorable predictions. Additionally, Fig. 4 indicates that a minimum of three flapping cycles is required to reveal a periodic lift trend showcasing the changes. The COMSOL simulation does not use the turbulent model because of the zero upstream velocity and small Reynolds number of the fluid.

Notably, the periodic changes increased with the number of meshes, particularly in the Extra Fine mesh configurations where in, the lift trend demonstrated the most periodic changes with smaller disturbances to the lift waveforms. Under the limited computing power of the multicore computer, the 67,328 extra-fine meshes required approximately 154 h and 43 min to calculate 8 flapping cycles.

Using a time-dependent solver, yielded an initial flap inclined angle of 20° and a flap stroke angle of 53° and 90°, are set up in advance. The three sets of boundary condition configurations for flapping frequency and wind tunnel entrance wind velocity were as follows: (1) 14 Hz and 1 m/s; (2) 15 Hz and 2 m/s; and (3) 15 Hz and 3 m/s, respectively. The simulation results indicated that when the flapping wing was situated in the wind tunnel and activated, the airflow around it and the corresponding lift were extremely chaotic. Running the simulation with three wind velocities demonstrated that the lift of the flapping wing displayed a more periodic change after 3 flapping cycles. Moreover, comparing the lift force values observed from the fore mentioned configurations were shown in Figs. 5 and 6. Fig. 5 revealed that the simulation with a wind velocity of 2 m/s for the stroke angle of 90° showed a higher average absolute lift

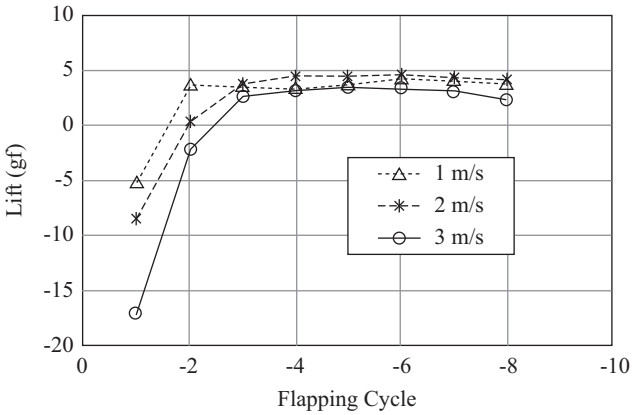

Fig. 5. Average lift values for different flapping cycles by COMSOL Multiphysics subject to a larger flapping stroke angle (90°); here, the lift denotes half flapping wing of Fig. 1 and the case of 2 m/s with 5 % fluctuation.

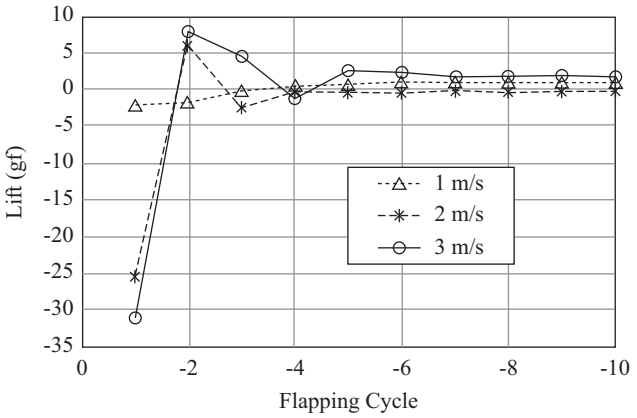

Fig. 6. Average lift values for different flapping cycles by COMSOL Multiphysics subject to a larger flapping stroke angle (53°); here, lift denotes half flapping wing of Fig. 1 and the case involving 3 m/s with 21% fluctuation.

with 5% fluctuation for the last 5 cycles, and the average total lift (8.76 gf; gram force) was close to the body mass of "Tamkang Humming bird" FWMAV (9.62 g) (Yang et al., 2015). Fig. 6 indicates that the simulation with a wind velocity of 3 m/s for the stroke angle of 53° showed a higher average lift with 21% fluctuation for the last 6 cycles; however, its average total lift (3.95 gf) was less than the body mass of "Golden Snitch" FWMAV (5.9 g) (Shu, 2008; Yang et al., 2009, 2012, 2013, 2014). The transient lift data demonstrates that COMSOL Multiphysics underestimated the unsteady lift of FWMAV "Golden Snitch". Moreover, the lift simulation was more favorable for the case involving a larger flapping stroke angle (90°). The lift error or fluctuation generated using COMSOL Multiphysics became larger as the flapping angle because smaller.

III. FLOW PATTEN COMPARISON BETWEEN NUMERICAL AND WIND TUNNEL DATA

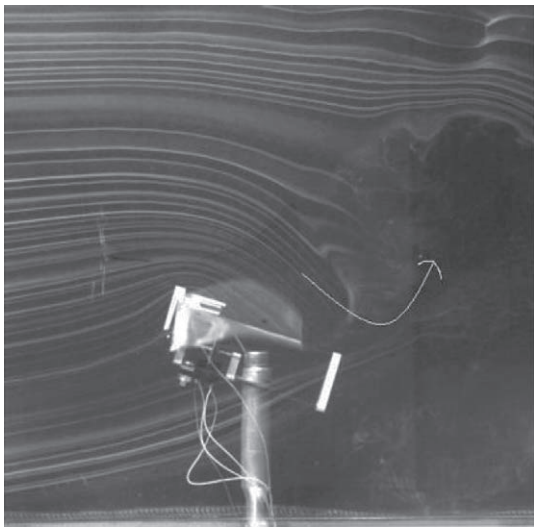

(a) Downstroke

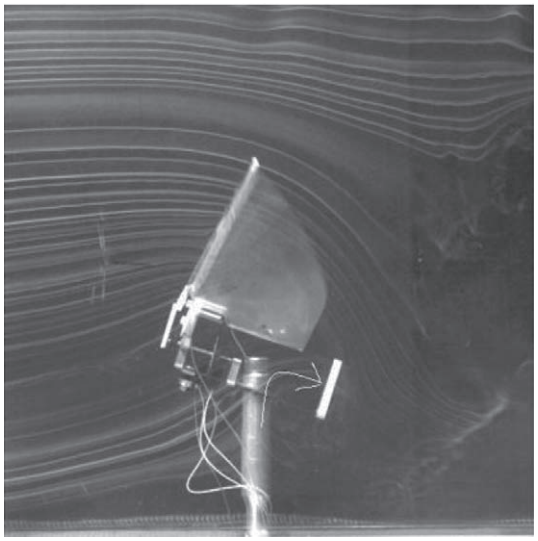

(b) Upstroke (Yang et al., 2017)

Fig. 7. Vortex (smoke line) of the "Golden Snitch" flapping wings (inclined angle = 20°; stroke angle = 53°; upstream velocity = 1 m/s; flapping frequency = 14 Hz.).

Chen conducted a signal interception experiment on the FWMAV "Golden Snitch," using a six-axis force gauge and a high-speed camera to capture the flow field marked by smoke trace (Chen, 2010). After the experiment was completed, signal comparison was subsequently conducted using LabVIEW software as well as Phantom 675, an accompanying software for high-speed cameras recording smoke trace; subsequently, the lift and thrust signals of the FWMAV were obtained.

The smoke trace indicated an anticlockwise vortex pattern had formed above the trailing edge (T.E.) during the wing downstroke as shown in Fig. 7(a). Conversely, a clockwise vortex pattern was formed below the trailing edge during the wing upstroke as depicted in Fig. 7(b). The simulation was performed under the conditions as below: inclined angle of 20°, stroke

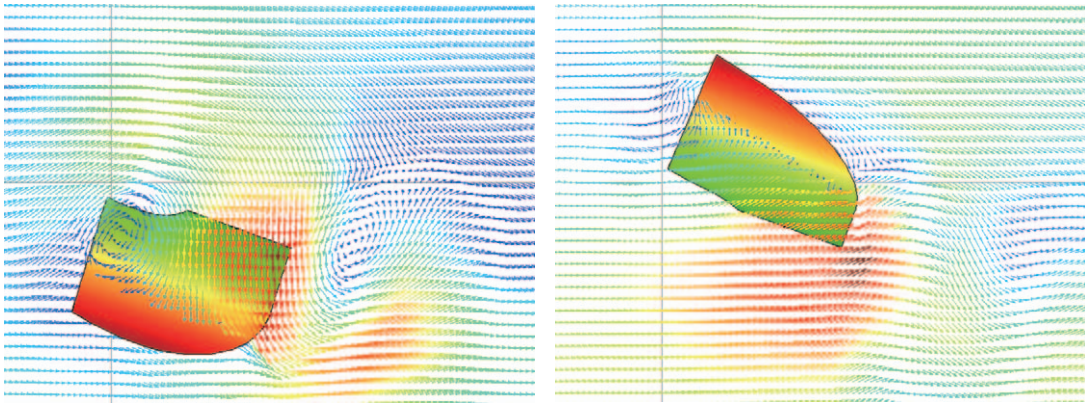

(a) Downstroke (b) Upstroke

Fig. 8. Vortex (CFD analysis) of the "Golden Snitch" flapping wings (inclined angle = 20°; stroke angle = 53°; upstream velocity = 1 m/s; flapping frequency = 14 Hz); Red, yellow, and green colors on the wing surface denote the maximum, median, and minimum displacements, respectively; red, yellow, and blue colors in the flow field denote the maximum, median, and minimum velocities, respectively (Yang et al., 2017).

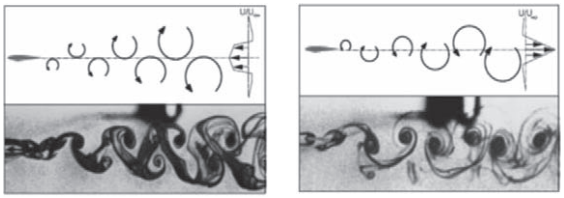

(a) drag (b) thrust

Fig. 9. Kármán vortex street display of thrust and drag force (von Kármán, 1963).

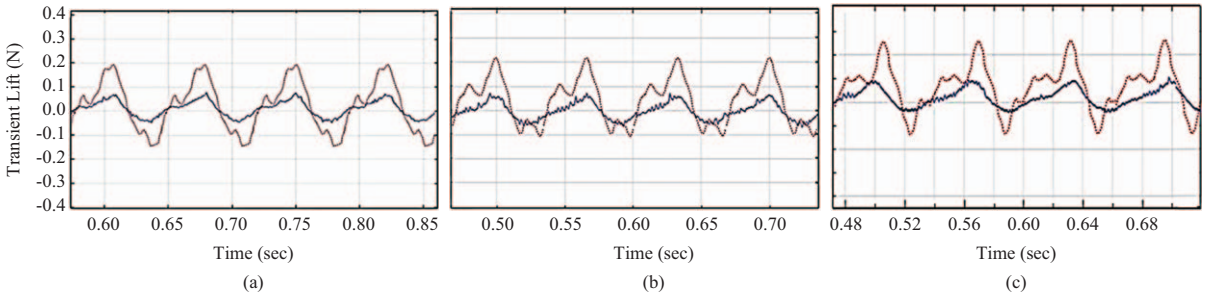

Fig. 10. Lift force diagram displaying four wing beat cycles of the flapping wing. The blue solid lines represent the simulation results, whereas the brown dotted lines represent the measured values from the wind tunnel experiment using a six-axis force gauge (Chen, 2010). (a) The flapping frequency is 14 Hz; the flapping stroke angle is 53°; the wind tunnel entrance wind velocity is 1 m/s. (b) The flapping frequency is 15 Hz; the flapping stroke angle is 53°; the wind tunnel entrance wind velocity is 2 m/s. (c) The flapping frequency is 15 Hz; the flapping stroke angle is 53°; the wind tunnel entrance wind velocity is 3 m/s (Chen, 2010).

angles of 53°, upstream velocity of 1 m/s, and flapping frequency of 14 Hz. The simulated flow field in Fig. 8 adequately matches the smoke trace in Fig. 7, known as the reverse Kármán vortex street, a mechanism found by von Kármán to explain lift and thrust production (von Kármán, 1963). In the case of conventional fixed wings, clockwise vortices formed above the trailing edge and an anticlockwise vortex formed below the trailing edge, which produced a backward jet and led to the drag formation (Fig. 9(a)). Conversely, in the case of flapping wings for the present investigations, an anticlockwise vortex is formed above the trailing edge and a clockwise vortex is formed below the trailing edge, which produced a forward jet and led to the formation of thrust (Fig. 9(b)).

IV. AERODYNAMIC FORCE COMPARISON BETWEEN NUMERICAL AND WIND TUNNEL DATA

Fig. 10 depicts three lift force diagrams of a flapping wing which includes numerical simulations using the flapping stroke

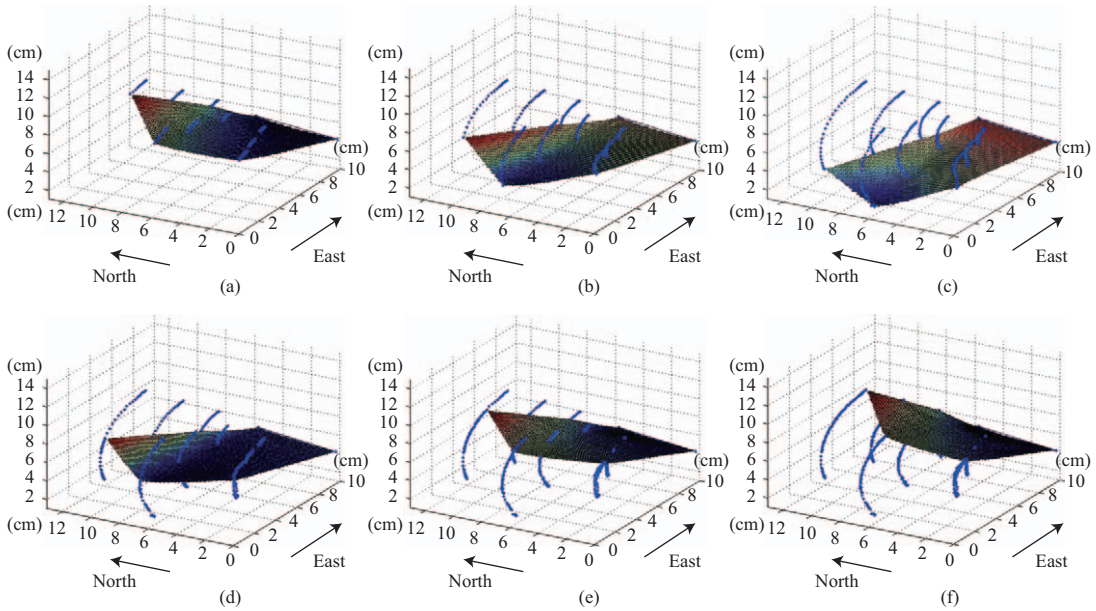

Fig. 11. 3D stereo photography of the wing surface of the "Golden Snitch" (Yang et al., 2013).

angle of 53°, the flapping frequency of 14-15 Hz, and the wind velocity of 1 m/s, 2 m/s, 3 m/s (blue solid line). It also includes the wind tunnel experimental values (brown dotted line) (Chen, 2010). Notably, the flapping lift measured by the 6-axis force gauge in the wind tunnel experiment shared similar characteristics partially with that of the numerical simulation, with both displaying a large and small peak (bi-peak) in the positive lift stage. A similar but weakened "bi-peak" phenomenon was again observed during the negative lift stage in the wind tunnel experiment, whereas the simulation result by COMSOL Multiphysics in this work did not show this feature.

Although the downstroke and upstroke motions of the flapping wing were designed with the same stroke distance, the wave patterns of positive and negative lift were not symmetrical. Within a single cycle in Fig. 10, the time duration ratio of the downstroke and the upstroke acquired from both the experiment and simulation was approximately 6:4. This value was confirmed by the high-speed photography results, wherein the duration of the downstroke was longer than that of the upstroke. In addition, the peak amplitude of positive lift was larger than that of negative lift in both the experimental and numerical cases. The ratio of maximal positive lift to maximal negative lift in the wind tunnel was approximately 1.4, whereas the simulation obtained a ratio of 1.6.

The lift phenomenon depicted in Fig. 10 shows that negative lift at the beginning of the downstroke became positive lift within a short timeframe. The lift increased continuously and reached its first peak at approximately 1/8 of the cycle (e.g., 0.48 s in Fig. 10(c)), after which it slowly declined and then increased again to the highest peak before the end of the downstroke (e.g., 0.50 s in Fig. 10(b) or 0.505 s in Fig. 10(c)). The subsequent decline from this peak simultaneously marked the end of the downstroke and the beginning of the upstroke. The lift gradually became negative before reaching a minimum at approximately 3/4 of the cycle. After a slight recovery, the lift reached a second minimum at approximately 7/8 of the cycle and attained its maximum negative value (e.g., 0.635 s in Fig. 10(a) or 0.525 s in Fig. 10(c)).

By restating the bipeak waveform of lift in Fig. 10, the waveform is more precisely obtained in the measured lift for the wind tunnel experiment. The timing of its highest peak and lowest minimum are comparable to that in the waveform of the numerical simulation with monotonously up-and-down features, which can be explained by the first lift mechanism's "delayed stall" of flapping (Dickinson et al., 1999). This translational lift mechanism achieves the largest lift peaks for the downstroke (e.g., 0.27 N at 0.505 s in Fig. 10(c)) and upstroke (e.g., 0.13 N at 0.525 s in Fig. 10(c)), respectively. The positive lift peak of 0.27 N is greater than the negative lift peak 0.13 N because of the 20° inclined angle of the FWMAV body. The positive AOA during the downstroke always has a larger magnitude than the negative AOA during the upstroke. Hence, the global net lift for a full cycle is positive and also supports the weight of FWMAV.

In addition to the translational lift, a rotational lift exists that is part of the measured lift and is due to the wing motion of stroke reversals. In addition to the stroke reversal characteristics, a counterclockwise pronation was observed at the beginning of the downstroke and a clockwise supination occurred at the beginning of the upstroke. This is analogous to the Magnus effect and is known as "rotational circulation," the second lift mechanism of flapping (Dickinson et al., 1999). Moreover, there is an additional lift mechanism, namely the "wake capture" of flapping (Dickinson et al., 1999).

However, the rotational lift of Dickinson's second and third mechanisms is not found in the numerical simulation data of this study. The kinematic reason for this will be discussed in

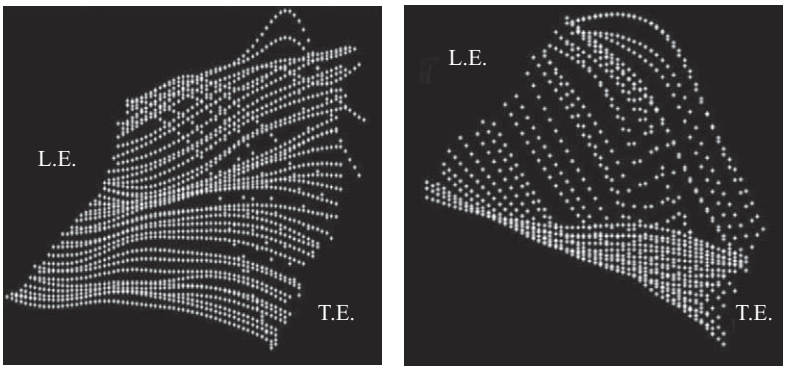

(a) Downstroke (a) Upstroke (Yang et al., 2014)

Fig. 12. 2D profile diagram of the wing surface center line of the "Golden Snitch" from Fig. 11; L.E. and T.E. denoting leading edge and trailing edge, respectively.

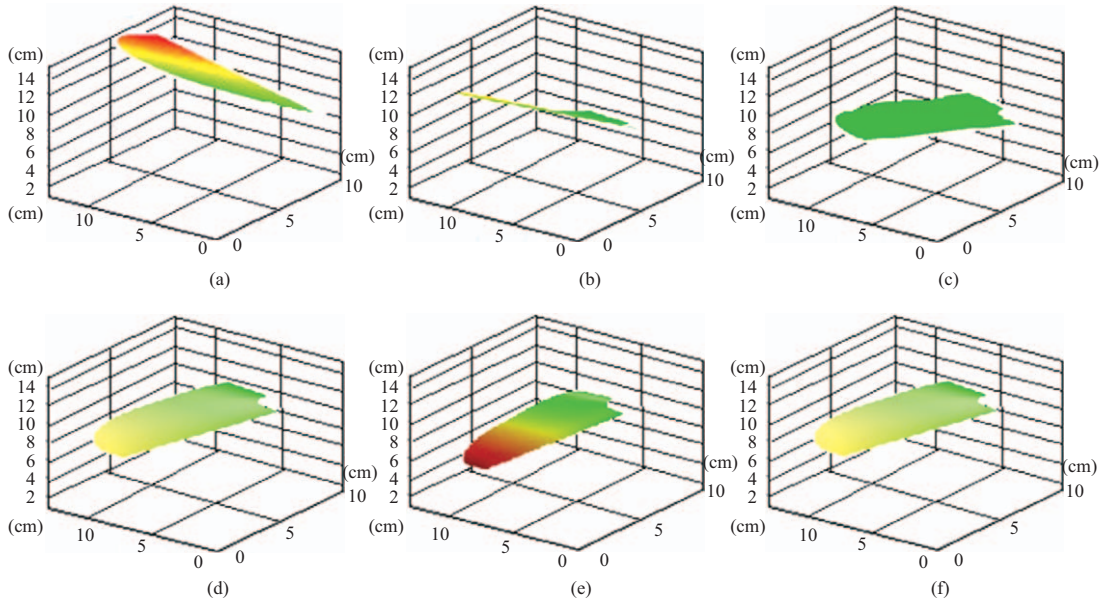

Fig. 13. 3D simulation of the flapping wing surface of the "Golden Snitch."

the next section. Although there is an excess lift contribution beyond the simulation wave form from the "bipeak" measured data in Fig. 10, the rotational lift contribution appears veiled and is comparable or coupled to the wing inertia plugging force (Sun et al., 2002). The excess lift waveform or "bipeak" phenomenon in Fig. 10 must be further investigated either experimentally or numerically in the future.

V. WING PROFILE COMPARISON BETWEEN NUMERICAL SIMULATION AND 3D TRAJECTORY USING STEREO-PHOTOGRAPHY

Figs. 11 and 12 illustrate the experimental data on the wing surface of the FWMAV "Golden Snitch," which was obtained using 3D stereo photography and Kwon3D software. The flexibility of the overall flapping wing typically results in deformation of the FWMAV through the membrane of the PET wing and carbon fiber spar at the leading edge of the wing (Yang et al., 2013, 2014). The measured kinematic information resulted in detailed, dynamic, wing profiles including stroke reversals and aeroelastic deformation.

Images of a 3D simulation using COMSOL Multiphysics of the wing surface of the "Golden Snitch" for one cycle of flapping motion are presented in Fig. 13. Because of the limitations of using COMSOL Multiphysics to assign different materials for the wing in Fig. 1, the carbon fiber at the leading edge could be only configured as PET, the same material as the wing membrane. In addition, the predescribed upstroke and downstroke sinusoidal motions were applied to the leading edge spar of the wing (in Step 13 of Table 2), which was equivalent to the motion of a rigid body with displacement but without deformation. The 3D flow obtained using COMSOL Multiphysics was therefore unable to exactly reflect the flapping wing profile observed

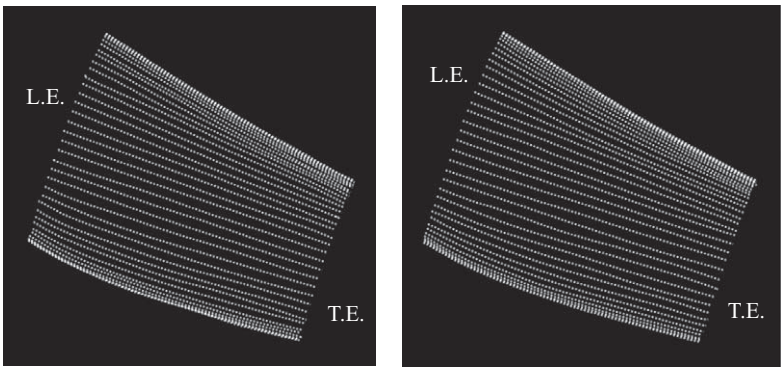

(a) Downstroke (a) Upstroke (Yang et al., 2014)

Fig. 14. 2D profile diagram of the wing surface center line of the "Golden Snitch".

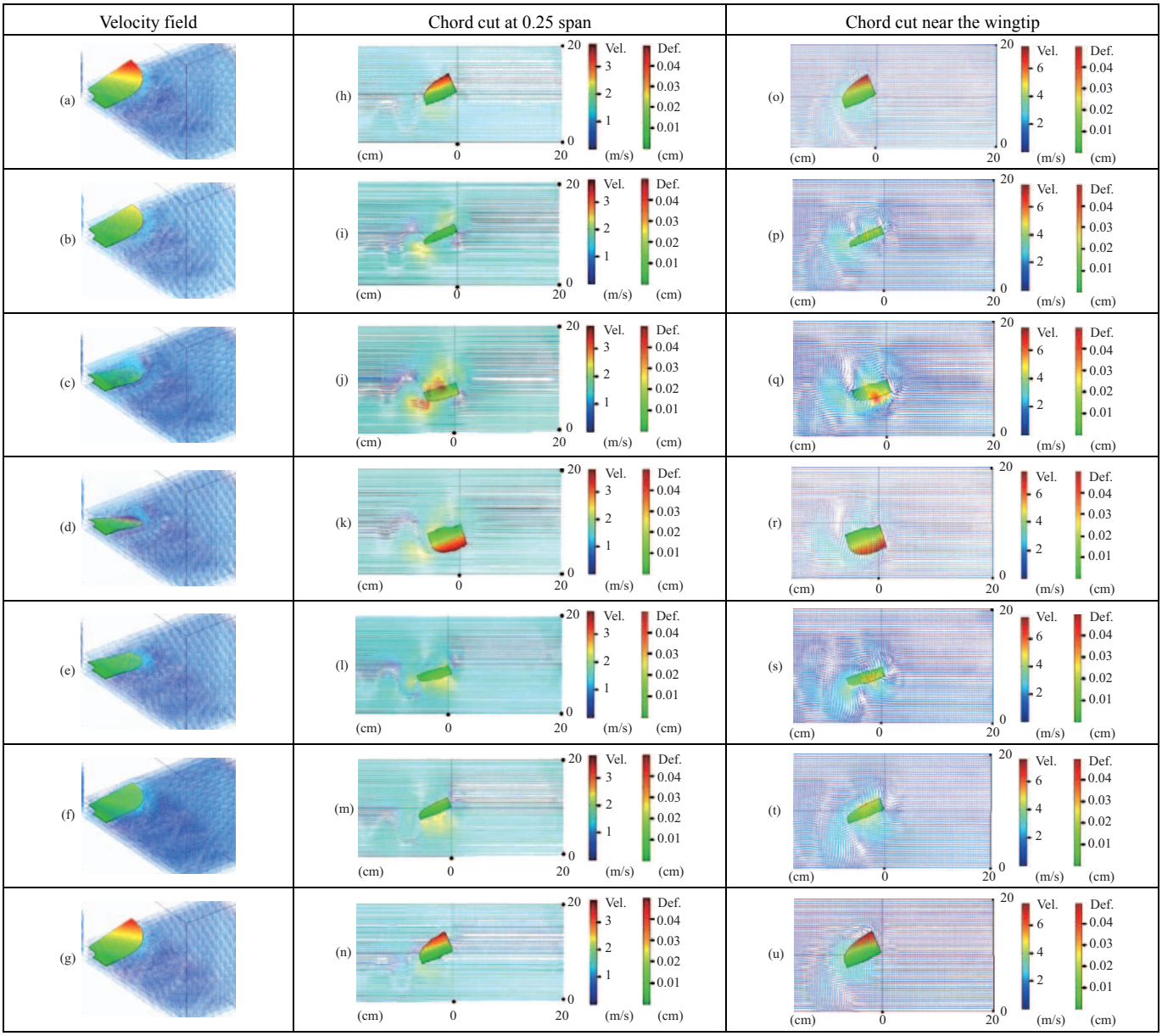

Fig. 15. 3D flow structure plots for a wind speed of 1 m/s and flapping frequency of 14 Hz: (a-g) velocity field; (h-u) intercepting streamwise cross section.

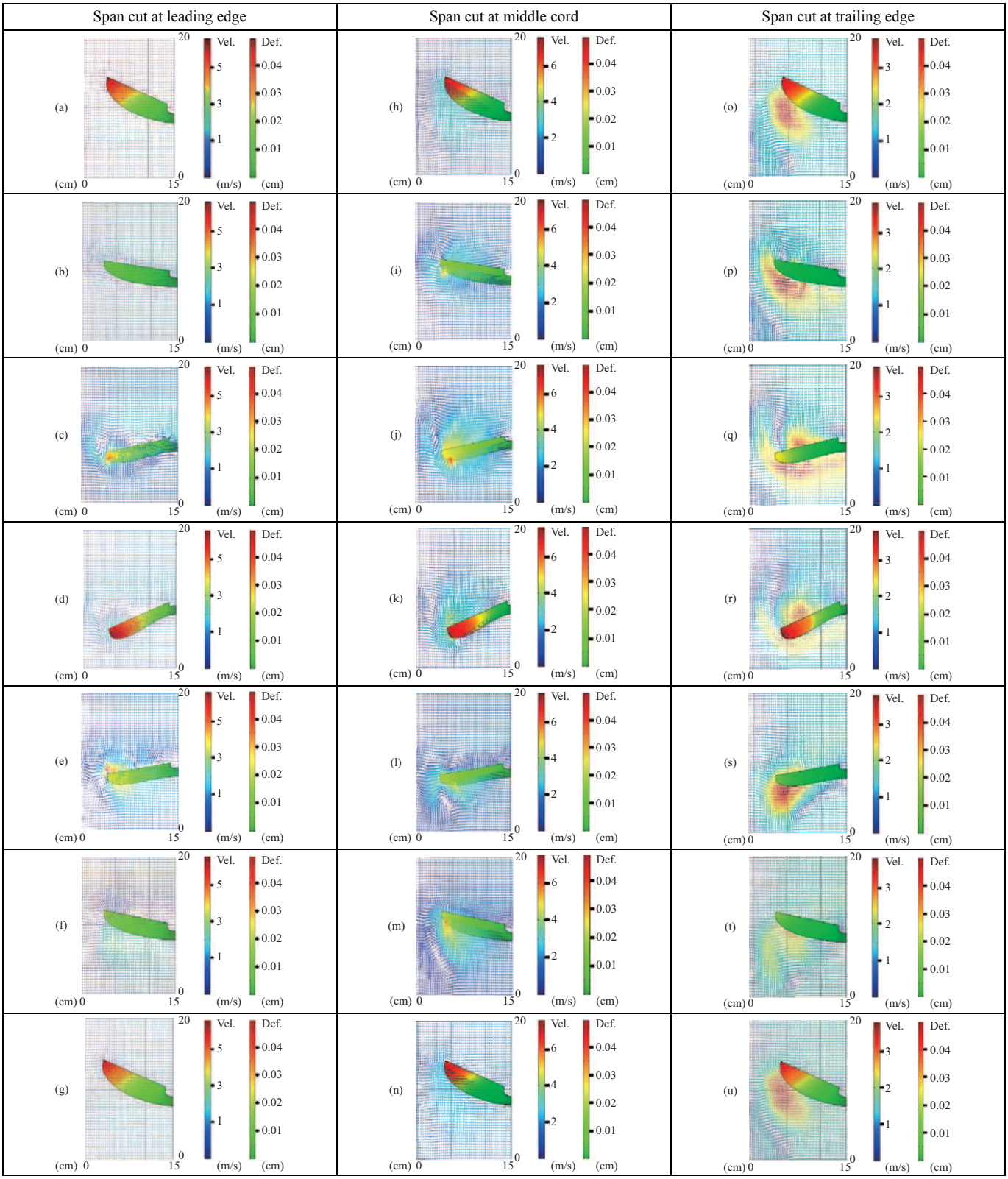

Fig. 16. 3D flow structure plots for a wind speed of 1 m/s and flapping frequency of 14 Hz: (a-u) intercepting spanwise cross-sections at three chord positions.

in Figs. 11 and 12 (Shu, 2008; Chen, 2010; Yang, 2012). The FSI function in COMSOL Multiphysics was only able to investigate elastic deformation of the PET wing membrane.

Fig. 14 indicates that the simulated wing profiles obtained

using COMSOL Multiphysics only include FSI to a very limited extent in this study. Compared with the rapidly changing wing profile in Fig. 12, the wing profiles in Fig. 14 move up and down with only a small negative camber. That is, the sinusoidal time-varying boundary setting of the wing leading edge was passively accounted for in the simulation without streamwise vibration or pronation/supination. However, the wing deformation profiles shown in Figs. 13 and 14 also failed to predict the positive-camber pattern that should be visible during the stroke reversal moments observed in Figs. 11 and 12. This may explain the difference in lift between the measured data and numerical simulation data in Fig. 10.

The following text explains the significant difference between the simulation and measured data in Fig. 10 based on the aforementioned kinematic investigation.

First, the lack of the wing trajectory of stroke reversal in Figs. 13 and 14 indicates that the corresponding numerical simulation underestimated the contribution from the rotational lift, which often accounts for 35% of the total flapping lift (Dickinson et al., 1999). Second, a lack of positive camber in the wing profile in Figs. 13 and 14 also indicates less lift in the simulation compared with the experimental measured data; less lift is apparent for the negatively cambered wing based on potential flow theory.

To demonstrate the consistency of the 3D flow analysis of a flapping wing, the pressure, net thrust, and streamline data will be discussed in the future. Fig. 15 (Fig. 16) shows the 3D velocity field during a full flapping cycle with intercepting planes in the streamwise (spanwise) direction. The color bars of "Vel." and "Def." denote the units and magnitudes of the velocity and wing deformation.

The reverse Kármán vortex sheets can be observed at different chord cuts in Fig. 15. The velocity magnitude and vortex pattern are easier to discern the wingtip cut rather than the 0.25 chord cut. The streamwise flow cuts of the 3D analysis are basically similar, except for the large air jet in Figs. 15(q) and 15 s. In addition, the wingtip vortex and downwash distribution are observed in all cases in Fig. 16. Some larger air jets are seen in Figs. 16(c), 16(e), 16(i), 16(j), and 16(m). In summary, the 3D flow simulation provides considerably more advantages than the 2D flow simulation.

VI. CONCLUSIONS

The following conclusions can be drawn from the present CFD analysis of the 3D flapping wing profile.

1. The powerful computation abilities of the COMSOL Multiphysics finite element environment in analyzing FSI enabled creating a 3D simulation of a flapping wing that was very similar to a real wing. According to the calculated time dependence value and convergence level, the results indicated that a flapping wing requires at least three flapping cycles after actuation to attain a periodic flow field change.
2. According to the lift trend diagram, periodic changes increased with the mesh numbers. The 67,328 finer meshes required 154 hours and 43 mins to calculate eight flapping cycles due to the limitations of multicore hardware computing capability.
3. Better average lift was achieved when the flapping wing had a stroke angle of 90°, flapping frequency of 14-15 Hz, an inclined angle of 20°, and a wind velocity of 2 m/s.
4. According to the 3D simulation of the flapping wing flow field, as well as the images of the smoke-tracking experiment in the wind tunnel, the reverse Kármán vortex street, which was also the thrust source of the flapping wing is observed.
5. The COMSOL Multiphysics 3D flow field was unable to exactly simulate the flapping phenomenon because the FSI function could simulate aerodynamic deformation of only the PET wing membrane. The simulation results for the lift underestimate the contribution of rotational lift, which often accounts for 35% of the total lift for flapping wings. In addition, the lack of positive camber in the wing profiles in the simulation implies that less lift was obtained in the simulation compared with the experimental measured data.
6. The streamwise and spanwise wing tip vortex flow patterns and downwash were observed in the simulation.

In summary, this work focuses the research on 3D flow simulation of flapping MAVs or natural flyers using COMSOL Multiphysics. Further investigations on this topic are required in the future.

ACKNOWLEDGEMENTS

The authors sincerely thank the financial support from Ministry of Science and Technology (MOST-106-2221- E-032-040) Taiwan and the help from Mr. Ting-Hsiung Huang.

REFERENCES

Bucur, D. M., G. Dunca, S.-C. Georgescu and A.-M. Georgescu (2016). Water flow around a flapping foil: preliminary study on the numerical sensitivity. U.P.B. Scientific Bulletin, Series D: Mechanical Engineering, 78(4), 175-182.

Chen, H.-C. (2010). Research on the semi-automatic data acquisition of MAV wind tunnel testing. Master's Thesis, Department of Mechanical and Electro-Mechanical Engineering, Tamkang University.

Chuang, S.-W., F.-L. Lih and J.-M. Miao (2012). Effects of Reynolds number and inclined angle of stroke plane on aerodynamic characteristics of flapping corrugated airfoil. Journal of Applied Science and Engineering 15, 247-256.

de Croon, G. C. H. E., M. A. Groen, C. De Wagter, B. D. W. Remes, R. Ruijsink and van B. W. Oudheusden (2014). Design, aerodynamics, and autonomy of the DelFly. Bioinspiration and Biomimetics 7, paper no. 025003.

Dickinson, M., F. Lehmann and S. Sane (1999). Wing rotation and the aerodynamic basis of insect flight. Science 284, 1954-1960.

Hubel, T. Y. and C. Tropea (2010). The importance of leading edge vortices under simplified flapping flight conditions at the size scale of birds. The Journal of Experimental Biology 213, 1930-1939.

Keennon, M., K. Klingebiel, H. Won and A. Andriukov (2012). Tailless flapping wing propulsion and control development for the Nano Hummingbird micro air vehicle. Proceeding of American Helicopter Society Future Vertical Lift Aircraft Design Conference, San Francisco, California, 1-24.

Kumar, A., C. Kaur and S. S. Padhee (2016). Analysis and optimization of dragonfly wing, Proceedings of the 2016 COMSOL Conference (User Pre-

sentations) in Bangalore, India.

Mellinger, D., M. Shomin and V. Kumar (2010). Control of quadrotors for robust perching and landing. Proceedings of the International Powered Lift Conference, Philadelphia, USA, 205-225.

Niu, Y.-Y., Liu, S.-H., Chang, C.-C. and Tseng, T. I. (2012). A preliminary study of the three-dimensional aerodynamics of flapping wings. Journal of Applied Science and Engineering 15, 257-263.

Nokia Bell Labs Team (2017) COMSOL Multiphysics Simulation 2017, IEEE Spectrum, Oct., 5.

Phan, H. V. and H. C. Park (2015). Remotely controlled flight of an insect-like tailless flapping-wing micro air vehicles. Proceedings of the 12th International Conference on Ubiquitous Robots and Ambient Intelligence (URAI), 315-317.

Pornsinsirirak, T. N., Y. C. Tai, H. Nassef and C. M. Ho (2001). Titanium-alloy MEMS wing technology for a micro aerial vehicle application. Sensors and Actuators A: Physical 89, 95-103.

Shu, C.-K. (2008). Research on the semi-automatic data acquisition of MAV wind tunnel testing. Doctoral Dissertation, Department of Mechanical and Electro-Mechanical Engineering, Tamkang University.

Sun, M. and Tang, J. (2002). Unsteady aerodynamic force generated by a model fruit fly wing in flapping motion. The Journal of Experimental Biology 205, 55-70.

von Kármán, T. (1963). Aerodynamics. McGraw-Hill Book Company, New York, USA.

Wan, T. and C.-K. Huang (2008). Numerical simulation of flapping wing aerodynamic performance under gust wind conditions. Proceedings of the 26th Congress of International Council of the Aeronautical Sciences (ICAS 2008), Anchorage, USA, 5, 983-993.

Wang, Z. J. (2000), Two dimensional mechanism for insect hovering. Physical Review Letter 85. 2216-2219.

Yang, L. J., B. Esakki, U. Chandrasekhar, K. C. Hung and C. M. Cheng (2015). Practical flapping mechanisms for 20cm-span micro air vehicles. International Journal of Micro Air Vehicles 7, 181-202.

Yang, L.-J. (2012). The micro-air-vehicle *Golden Snitch* and its figure-of-8 flapping. Journal of Applied Science and Engineering 15, 197-212.

Yang, L.-J., A.-F. Kuo and C.-K. Hsu (2012). Wing stiffness on light flapping micro aerial vehicles. Journal of Aircraft 49, 423-431.

Yang, L.-J., C.-K. Hsu, H.-C. Han and J.-M. Miao (2009). Light flapping micro-aerial-vehicle using electrical discharge wire cutting technique. Journal of Aircraft 46, 1866-1874.

Yang, L.-J., F.-Y. Hsiao, W.-T. Tang and I.-C. Huang (2013). 3D flapping trajectory of a micro-air-vehicle and its application to unsteady flow simulation. International Journal of Advanced Robotic Systems 10, paper no. 264.

Yang, L.-J., H.-L. Huang, J.-C. Liou, B. Esakki, and U. Chandrasekhar (2014). 2D quasi-steady flow simulation of an actual flapping wing. Journal of Unmanned Systems Technology 2, 10-16.

Yang, L.-J., S. Marimuthu, K.-C. Hung, H.-H. Ke, Y.-T. Lin, and C.-W. Chen (2015). Development scenario of micro ornithopters. Journal of Aeronautics, Astronautics and Aviations 47, 397-406.

Yang L. J. (2017). The wind tunnel test and unsteady CFD of an ornithopter formation. (ed. by Bajpai and Chandrasekhar) Innovative Design and Development Practices in Aerospace and Automotive Engineering. Lecture Notes in Mechanical Engineering. Springer, Singapore.